Crystal-chemical and biological controls of trace and minor element incorporation into magnetite nanocrystals

Matthieu Amor[a*], *Damien Faivre*[a], *Daniel M. Chevrier*[a*]

[a] *Aix-Marseille Université, CEA, CNRS, BIAM, 13108 Saint-Paul-lez-Durance, France*

Keywords: Trace Element Partitioning, Magnetotactic Bacteria, Magnetite Nanoparticles, Biomineralization, Lattice and Crystal Field Theories

*To whom correspondence should be addressed:
matthieu.amor@cea.fr (MA); daniel.chevrier@cea.fr (DMC)

Abstract

Magnetite nanoparticles possess numerous fundamental, biomedical and industrial applications, many of which depend on tuning the magnetic properties. This is often achieved by the incorporation of trace and minor elements into the magnetite lattice. Such incorporation was shown to depend strongly on the magnetite formation pathway (i.e., abiotic *vs* biological), but the mechanisms controlling element partitioning between magnetite and its surrounding precipitation solution remain to be elucidated. Here, we used a combination of theoretical modelling (lattice and crystal field theories) and experimental evidence (high-resolution inductively coupled plasma mass spectrometry and X-ray absorption spectroscopy) to demonstrate that element incorporation into abiotic magnetite nanoparticles is controlled principally by cation size and valence. Elements from the first series of transition metals (Cr to Zn) constituted exceptions to this finding as their incorporation appeared to be also controlled by the energy levels of their unfilled 3d orbitals, in line with crystal field mechanisms. We then show that element incorporation into biological magnetite nanoparticles produced by magnetotactic bacteria (MTB) cannot be explained by crystal-chemical parameters alone, which points to the biological control exerted by the bacteria over the element transfer between MTB growth medium and the intracellular environment. This screening effect generates biological magnetite with a purer chemical composition than the abiotic materials formed in a solution of similar composition. Our work establishes a theoretical framework for understanding the crystal-chemical and biological controls of trace and minor cation incorporation into magnetite, thereby providing predictive methods to tailor the composition of magnetite nanoparticles for improved control over magnetic properties.

Main Text

Magnetite [$Fe(II)Fe(III)_2O_4$] is a naturally-occurring ubiquitous Fe oxide that can be precipitated through abiotic chemical reactions[1]. Microorganisms can also promote magnetite formation. Among them, only magnetotactic bacteria (MTB) are known to synthesize nanoparticles of magnetite in a genetically controlled manner by incorporating Fe into organelles called magnetosomes for magnetite formation[2]. MTB are proposed to represent some of the most ancient microorganisms on Earth[3], and are markers of oxic/anoxic transitions in the environment[4]. Nanoparticles of magnetite are of fundamental scientific interest in industrial and biomedical applications[5,6,7], with many of these interests relying on careful tuning and optimization of magnetic properties. A particular way of doing so directly relies on modifying the chemical composition of magnetite, into which cations can substitute for Fe, incorporating into the magnetite lattice structure and thereby modifying its magnetic properties such as coercivity, saturation magnetization or heat release capacity[8,9]. Cation incorporation has been shown to depend strongly on the nature of the magnetite formation pathways (i.e., abiotic or biologic)[10], but the mechanisms controlling such incorporation remain unknown.

The content of trace and minor elements in magnetite is also of critical interest for the detection of extra-terrestrial and ancient terrestrial life[4] as exemplified by the controversial origin of magnetite in the Martian meteorite ALH84001[11]. This meteorite contains nanocrystals of magnetite encapsulated in (Ca, Mg, Fe)-carbonates showing a pure chemical composition (i.e., they contain no detectable dopant elements)[12]. They were proposed to be produced from the thermal decomposition of the carbonate matrix[13], although laboratory experimentation showed that incorporation of Mg and Ca into the generated magnetite should occur during such processes[14]. An alternative biological origin of this Martian magnetite was thus suggested, since only MTB were shown to generate magnetite with pure chemical composition[10]. Such unique property of biological magnetite was proposed as a reliable tool for the identification of fossils

63 of MTB in ancient terrestrial and extra-terrestrial environments[4]. Therefore, understanding the
64 mechanisms leading to trace and minor element incorporation into magnetite, as well as the
65 capacity of MTB to screen for element incorporation, has important implications in exobiology
66 and (paleo)environmental sciences[4].

67 In the present study, we establish the crystal-chemical parameters controlling the
68 incorporation of trace and minor elements into magnetite nanocrystals. Using the
69 concentrations of chemical elements measured from high-resolution inductively coupled
70 plasma mass spectrometry (HR-ICP-MS)[10] in different series of abiotic magnetite, we show
71 that the cation incorporation is controlled by the ionic radius and the valence. We do report a
72 few exceptions: elements from the first series of transition metals (Cr, Mn, Co, Ni, Cu, Zn) are
73 more stabilized into the magnetite lattice during precipitation than predicted from their size and
74 valence. X-ray absorption microscopy (XAS) specifically on Mn, Co and Zn demonstrates
75 demonstrate that the preferential incorporation of first series transition metals can be explained
76 by the energy levels of unfilled 3d electron orbitals. Identifying this comprehensive framework
77 of the crystal-chemical processes controlling element incorporation into magnetite enables us
78 to investigate the biological control exerted by the magnetotactic strain *Magnetospirillum*
79 *magneticum* AMB-1 on element partitioning between magnetite and the external solution[10]. We
80 find that the behavior of elements during biological formation of magnetite cannot be explained
81 by crystal-chemical parameters alone: their incorporation into MTB magnetite is more limited
82 than expected given their ionic radius and valence. To establish the biological relevance of these
83 findings, we prepared additional cultures of the magnetotactic *Magnetospirillum*
84 *griphyswaldense* MSR-1, another model magnetotactic strain. HR-ICP-MS analyses of MSR-
85 1 magnetite and residual growth medium complemented with trace elements yielded element
86 partitioning similar to that observed in AMB-1, confirming a consistent application of
87 biological control over metal incorporation. Furthermore, XAS analyses evidenced no

alteration of dopant cation size and valence in biological magnetite. These results point towards and active screening of elements by the bacteria to limit the transfer of trace and minor elements from the external solution to internally formed magnetite nanoparticles. Finally, we discuss the implications of our work for fundamental, environmental and biomedical applications of magnetite nanoparticles.

Results and Discussion

Chemical composition of abiotic and biological magnetite

Magnetite possesses an inverse spinel structure, with trivalent cations [Fe(III)] contained in both octahedral (6-coordination) and tetrahedral sites (4-coordination) while divalent cations [Fe(II)] occupy octahedral sites only[1]. During abiotic or biological formation, distinct trace and minor cations can substitute Fe(II) or Fe(III) by incorporating into the lattice structure. A previous study quantified the trace element content of abiotic and biological (AMB-1 strain) magnetite nanoparticles[10]. Magnetite nanoparticles were thoroughly purified in order to eliminate adsorbed elements. X-ray diffraction and high-resolution electron microscopy analyses of the samples revealed pure magnetite crystals, with no additional precipitated phases potentially induced by element doping[10]. The concentrations of trace and minor elements (X) in magnetite and in the residual solution after nanoparticle formation were measured using HR-ICP-MS. For each element, a partition coefficient (D^X) between magnetite and solution was calculated from the equation:

$$D^X = \frac{[X_{magnetite}]}{[X_{solution}]} \quad (1)$$

where $[X_{magnetite}]$ and $[X_{solution}]$ are the massic concentrations of an element X in magnetite and in the residual solution after precipitation, respectively, expressed in ppb. Thus, the partition

coefficient quantifies the capacity of an element to incorporate into magnetite and does not depend on the initial concentration of trace elements in the precipitation solution, at least in first approximation. We show below that element partitioning can be explained by crystal-chemical parameters according to established models, demonstrating that the element concentration used (100 ppb for each element) did not induce competition between elements for incorporation into magnetite. The same set of partition coefficients was calculated in the case of biological formation by AMB-1 with identical dopant concentrations in the initial study[10]. Elemental concentrations in the residual growth media as well as magnetite samples thoroughly purified were quantified using HR-ICP-MS. Measured elemental concentrations and partition coefficients are given in Tables S1 and S2.

We demonstrate below (see sections on the lattice strain theory and crystal field theory) that elements from the first series of transition metals (Cr, Mn, Co, Ni, Cu and Zn) behave in a distinct manner from other metal groups. To better understand the mechanisms leading to their incorporation during magnetite precipitation, we produced additional abiotic and biological (strain MSR-1) samples doped with a Mn/Co/Zn mixture. The redox state and coordination of Fe, Mn, Co, Zn in magnetite was determined using XAS. Analyses of Ni and Cu doping were also conducted, but the dopant metal concentration in biological magnetite samples was too low (Fig. S1), similar way to what has been reported for MSR-1[15]. Transmission electron microscopy and XAS characterization at the Fe K-edge of the magnetite samples are presented in Fig. 1. XAS spectra show that the produced material corresponds to magnetite via the close alignment of three near-edge features in addition to post-edge oscillations.

Lattice strain control of element incorporation into magnetite

The partitioning of a trace element between a given lattice site (M) and melts under high temperature and pressure conditions is controlled by the ion radius and valence[16]. For a given

valence (n+, with n = 1, 2, 3 or 4), incorporation of a trace element is maximized when the ionic radius (r^X) matches the size of the site M ($r_{n+}^{0(M)}$). A shift from this ideal size generates an elastic deformation that is accommodated by the neighboring crystal lattice, translating into a penalty in energy for the ion incorporation and, consequently, into a decrease of D^X. A size shift of the same magnitude but with opposite sign corresponds to the same energy penalty. The distribution of D^X values for an isovalent series of elements thus follows a parabolic trend with a maximum value ($D_{n+}^{0(M)}$) corresponding to a fictive element perfectly matching the size of the lattice site (i.e., strain-compensated D^X)[16] (see Eqs. 2 and 3 in Materials and Methods). Similarly, heterovalent cation substitution entails accommodation of excess electric charge by the crystal lattice that will also translate into a penalty in energy for element incorporation[16]. Thus, $D_{n+}^{0(M)}$ corresponding to each valence also follow a parabolic trend with a maximum coefficient $D^{00(M)}$ corresponding to an ion causing no electrostatic charging (i.e., homovalent substitution).

We tested such a model in the case of magnetite to determine the role of ion radius and valence in the distribution of D^X but under different conditions at ambient temperature and atmospheric pressure. For all valences, the experimentally determined D^X plotted against their cation radius were close identical to the predicted values calculated from Eq. 2. This shows that the incorporation of most trace and minor elements into abiotic magnetite can be predicted by a lattice strain model. The strain-compensated $D_{n+}^{0(M)}$ extracted from Fig. 2 and represented against ionic charge also followed the expected parabolic trend (Fig. 3) (Eq. 3 in Materials and Methods). The maximum $D_{n+}^{0(M)}$ corresponding to $D^{00(M)}$ was observed for a cation charge of +2.7, almost identical to the bulk Fe valence in magnetite (+2.67). Overall, the distribution of D^X values determined experimentally in abiotic precipitation followed a lattice strain model, demonstrating that cation radius and valence control the incorporation of trace and minor

elements in abiotic magnetite. However, a few exceptions were observed: Cr(II), Cr(III), Mn(II), Co(II), Ni(II), Cu(II) and Zn(II) (grey circles in Fig. 2), which all belong to the first series of transition metals (3d metals) also containing Fe, showed higher D^X than expected from their radii and valence. Such preferential incorporation cannot be explained by potential co-precipitation of distinct (oxyhydr)oxides phases as shown by X-ray and diffraction and electron microscopy performed on the samples used for the determination of D^X[10].

Next, we consider the partition coefficients of trace and minor elements between the biological magnetite and the growth medium, which shows a distinct picture from abiotic results (Fig. 2). D^X values were consistently lower than those predicted from a lattice strain model (Eq. 2). Such depletion corresponds to a factor of ~5 x 10^1 [Cs(I)] up to ~9 x 10^7 [La(III)]. The range of variation for D^X was also narrower in the case of biological magnetite, with most values ranging between 10^{-1} and 10^2, compared to the D^X variation in abiotic magnetite of 7 orders of magnitude (Rb to Bi). Finally, the distribution of partition coefficients could not be modeled by the lattice strain theory using Eq. 2, showing that crystal-chemical parameters cannot explain the partitioning of trace and minor elements between AMB-1 magnetite and the external growth medium.

Crystal field constraints on element incorporation into magnetite and coordination of 3d metals in magnetite

Elements from the first series of transition metals, including Fe, possess unfilled 3d orbitals in at least one of their oxidation sates[17]. The two sets of 3d orbitals, namely t_{2g} (i.e., d_{xy}, d_{xz}, d_{yz}) and e_g (i.e., d_{z^2} and $d_{x^2-y^2}$), have different geometries with the electronegative charge pointing to distinct directions. In octahedral configuration, electrons from e_g orbitals directly face the negatively charged oxygen, which maximizes the electric repulsion and thus corresponds to more energetic configurations[17]. The opposite case is observed in tetrahedral

coordination. The origin and consequences of these electrostatic interactions on the energy levels of 3d orbitals is described by the crystal field theory[17]. For each element of a given valence, the crystal field stabilization energy (CFSE) was documented by McClure in octahedral and tetrahedral coordination[18]. The partitioning of Cr(II), Cr(III), Mn(II), Co(II), Ni(II), Cu(II) and Zn(II) during abiotic magnetite precipitation was modeled from their CFSE for both coordination configurations (Fig. S2). No clear correlation between $\log D^X$ and CFSE values was observed, suggesting that coordination and/or valence of doping elements are not as expected. This needed to be confirmed to determine whether crystal field effects control the incorporation of 3d metals in magnetite.

We determined the coordination and valence of Mn, Co and Zn using XAS in both abiotic and biological magnetite. Abiotic syntheses and MSR-1 cultures were performed in the presence of Mn(II), Co(II) and Zn(II) under the same experimental mixed-doping conditions as described above for AMB-1. The D^X values corresponding to abiotic precipitation were almost identical to those previously obtained (see Tables S1 and S4), but D^X values obtained from MSR-1 were higher than those previously obtained with AMB-1 (Tables S2 and S4). Such discrepancy can be explained by the magnetite yield and intracellular Fe content in the two strains, where MSR-1 is known to incorporate more iron than AMB-1 under standard growth conditions used in the present contribution[19]. An increased mass of magnetite increases the total mass of trace elements contained in magnetite, which in turn decreases the concentrations of trace elements in the residual medium and lead to an increase of D^X. We thus calculated partition coefficients of Mn, Co and Zn normalized to Fe ($D^{X/Fe}$) to compare values obtained from AMB-1 and MSR-1. They yielded similar results in both strains (Table S5).

Abiotic and biological magnetite samples were measured in powdered form at the respective dopant K-edges to confirm the site occupancy of doped metals in magnetite. Due to the dopant-level concentration of each metal in magnetite, fluorescence detection was employed to collect

XAS spectra. In the case of Co for abiotic magnetite nanoparticles, the fluorescence signal was too weak to collect usable spectra, which is understandable given the ten-fold lower Co concentration abiotic in magnetite relative to Mn and Zn (see Table S4). Nevertheless, from similar previous characterizations of Co-ferrite nanoparticles ($Co_xFe_{3-x}O_4$) prepared via different synthetic methods, Co is well known to occupy mainly octahedral sites[20,21]. K-edge XAS for Mn-doped abiotic magnetite shows an oxidation state between Mn(II) and Mn(III) when compared with Mn-based oxides (Fig. 4A). This is reflected by the position of both the pre-edge position and the main rising edge (Fig. 4A, inset). Near-edge features of Mn-doped magnetite correspond more so with a Mn-ferrite reference ($Mn_{0.5}Fe_{2.5}O_4$)[22] indicating similar chemical and structural environment. However, weaker pre-edge and post-edge features (6562 eV) potentially originate from the dilute and inhomogenous nature of the dopant metal in the magnetite lattice compared to the Mn-ferrite reference. The difference in relative peak intensities when compared to the reference material may also indicate a partial change in octahedral/tetrahedral site occupancy. Although the extended X-ray absorption fine structure (EXAFS) region is too weak to fit scattering paths for structural information, *ab initio* simulations of the Mn K-edge X-ray absorption near-edge structure (XANES) for tetrahedral and octahedral Mn substitutions in magnetite (Fig. S3) confirm near-edge absorption features from both $Mn_{0.5}Fe_{2.5}O_4$ reference and Mn-doped abiotic magnetite match with tetrahedral coordination. Zinc K-edge XAS for Zn-doped abiotic magnetite (Fig. 4C) has poorly defined near-edge features and very weak EXAFS. When compared with a Zn-ferrite reference ($ZnFe_2O_4$), known to have a normal spinel crystal structure with Zn(II) occupying tetrahedral sites, the width and positioning of the XANES aligns well but the specific near-edge features are less apparent. Linear combination fitting with Zn-based references revealed a contribution of $ZnFe_2O_4$ (41%) and octahedral Zn(II) complexes (59%) (Fig. S4). We attribute octahedral

Zn(II) complexes to be Zn sites allocated on the nanoparticle surface with short-range order or Zn(II) complexes adhered to the nanoparticle surface.

Higher quality data was obtained for biological magnetite, since dopants were found to be in higher concentration than in the abiotic samples, at least partially due to the high initial concentrations used in the bacterial growth media (Table S4). Cobalt K-edge XAS for Co-doped biological magnetite highly resembles that of a Co-ferrite reference ($CoFe_2O_4$) (Fig. 4B), given the identical energies of distinctive near-edge features. From known crystal structure of Co-ferrite nanoparticles[23,24], Co mainly occupies octahedral sites in magnetite in line with previous work on MTB[25,26]. Manganese K-edge XANES of Mn-doped biological magnetite is again similar to the $Mn_{0.5}Fe_{2.5}O_4$ reference (Fig. 4A), with peak positions and their relative intensities even more comparable. The higher data quality for this sample afforded supplemental EXAFS information and a well-resolved pre-edge region. Regarding the latter (Fig. 4A, inset) and remarking on simulations performed (Fig. S3), a second pre-edge feature is observable for Mn-doped biological magnetite (Fig. S3, see features i and ii) that can be attributed as a partial +3 valence state of the dopant[27]. EXAFS fitting yielded a Mn-O coordination number of 3.7 and a bond distance of 202 pm (Fig. S5 and Table S6), both suggesting a tetrahedral environment for Mn dopants is likely, consistent with another recent study[15]. Nevertheless, a small contribution of Mn-Fe single scattering from Mn in octahedral sites (coordination number 1.9, bond distance 299 pm) was found to complete EXAFS fitting of Mn-O and Mn-Fe (coordination number 13.1, bond distance 352 pm) scattering from Mn in tetrahedral sites.

Zn XANES features are more prominent for Zn-doped biological magnetite than for the abiotic case, with near-edge features more resembling the Zn-ferrite reference material (Fig. 4C). From linear combination fitting, we obtain 78% $ZnFe_2O_4$ and 22% octahedral Zn(II) complexes for the Zn-doped biological magnetite (Fig. S4), indicating a higher contribution of

Zn incorporated into magnetite with tetrahedral coordination. EXAFS fitting of Zn-O path yielded a coordination number of 3.9 and bond distance of 205 pm confirming Zn mainly occupy tetrahedral sites. In our case, we note a high incorporation of Zn into MSR-1 magnetite as normal spinel $ZnFe_2O_4$ from doping bacteria growth media with Zn(II), whereas another study found more ZnO than $ZnFe_2O_4$[15].

Using the experimentally determined coordination and valence of Mn, Co and Zn, a corrected CFSE was calculated. As mentioned above, Mn in abiotic magnetite showed mixed +2/+3 valence. The rising edge position (determined from the first derivative maximum of the main absorption edge) was shifted towards higher values when compared to the Mn-ferrite reference. This indicates more oxidized Mn in the abiotic magnetite samples than in the ferrite reference, which has been shown to contained 25% Mn(III) and 75% M(II)[28], while the biological magnetite overlapped the Mn-ferrite reference which suggests a similar valence for Mn. Therefore, the Mn(III) / total Mn ratios in the abiotic and biologic magnetite were taken as 0.3 (i.e., higher than Mn-ferrite reference) and 0.25 (i.e., similar to Mn-ferrite reference), respectively. Zinc coordination was considered to be 60% octahedral / 40% tetrahedral in the abiotic magnetite, and 20% octahedral / 80% tetrahedral in the biological nanoparticles based on the fitting results. Finally, Co was considered to mainly occupy octahedral sites based on the extensive literature[29,30] that is consistent with present Co-doped MSR-1 magnetite. Measured partition coefficients represented against XAS-corrected CFSE are shown in Fig. 5. In the abiotic case, $\log D^X$ values showed a weak linear relationship with CFSE (correlation coefficient of 0.87), while biological $\log D^X$ showed almost constant values with no correlation with CFSE (correlation coefficient of 0.006) (Fig. 5A). To take into account crystal field controls independently of lattice strain mechanisms, the measured partition coefficients in abiotic nanoparticles were normalized to the D^X predicted from lattice strain theory (Eq. 2 and Fig. 2). The results are presented in Fig. 5B and show a stronger linear correlation between the

286 trace element stabilization and the corrected CFSE (correlation coefficient of 0.99). Our results
287 thus demonstrate the importance of taking into account the actual coordination of trace 3d
288 metals in magnetite since their incorporation is controlled by crystal field mechanisms.
289
290 **Biological control over element transfer to magnetosomes in magnetotactic bacteria**
291 Our work aimed at understanding the mechanisms controlling the incorporation of cations
292 distinct from Fe into magnetite. It demonstrates that partitioning of trace and minor elements
293 between abiotic magnetite and surrounding solution is controlled by cation radius and valence,
294 as well as the energy levels of 3d orbitals for elements from the first series of transition metals
295 (Cr to Zn). The biological case showed a distinct picture as the distribution of D^X could not be
296 modeled from lattice strain and crystal field theories alone. The low partition coefficients and
297 low variation of D^X in the biological conditions are in line with the proposed hypothesis of Fe
298 biopurification during magnetite formation, establishing the chemical purity of magnetite as a
299 signature of MTB activity.
300 The variability induced by MTB on trace and minor element partitioning could arise from
301 the homeostasis of chemical conditions (pH, redox potential, etc.) in the intracellular
302 environment, which are distinct from the external solution and maintained by the metabolic
303 activity of the bacteria. They control the cation valence and speciation (and thus its size) in
304 solution, which may in turn shift element partitioning (Eqs 2 and 3, Figs. 2 and 3). As evidenced
305 by XAS measurements (linear fitting and comparison to references), the biological control over
306 magnetite nanoparticle formation enables more homogeneous incorporation of dopants into the
307 crystal lattice compared to the abiotic nanoparticles also produced under ambient conditions.
308 We hypothesize that such homogeneous incorporation of dopant elements in biological
309 magnetite could be due to the slow formation of magnetite in MTB (3 days of growth) compared
310 to the abiotic nanoparticles which precipitates as soon as the pH conditions are favorable (see

311 materials and methods). However, the variability of cation size and valence evidenced by XAS
312 measurements is too low to account for the decrease of D^X in the biological conditions (up to
313 7 orders of magnitude, see Fig. 2)

314 Although not demonstrated, the lower levels of doped cations in biological magnetite were
315 discussed as being caused by active and selective Fe incorporation into magnetosomes that
316 excludes distinct elements[10]. Magnetite in MTB precipitates from a medium contained in lipid
317 vesicles that is physically separated from the external solution and isolated from doping
318 elements (i.e., the bacterial growth medium), diminishing their level of incorporation. A notable
319 difference between both conditions of magnetite precipitation is the remarkable decrease of
320 partition coefficients in bacterial cultures as all elements showed lower D^X values than those
321 predicted from the lattice strain theory (Fig. 2). As detailed in the above section, an increased
322 Fe precipitation into abiotic magnetite (i.e., a higher D^{Fe} partition coefficient) compared to
323 biological conditions would lead to an increase of D^X. However, the decrease of D^{Fe} in the
324 biological conditions when compared to abiotic syntheses is too limited to account for the low
325 D^X in AMB-1 and MSR-1 cultures (Fig. 2 and Table S4). This was also demonstrated in
326 previous work discussing the distribution of partition coefficients normalized to Fe[10].

327 The range of partition coefficients was also narrower in AMB-1 cultures compared to abiotic
328 magnetite (Figs. 2 and 6). Consequently, the enrichment of trace elements in AMB-1 magnetite
329 quantified by the ratio of measured D^X normalized to D^X values predicted from the lattice
330 strain theory decreases linearly with the increase of cation radius, up to the ideal size ($r_{n+}^{0(M)}$)
331 that is associated with the maximum D^X (Fig. 6). Enrichment of doping elements in MTB
332 magnetite then increases again for cation radii higher than $r_{n+}^{0(M)}$ (Figs. 6A and 6D).
333 Accordingly, the depletion of trace and minor elements from MTB magnetite is higher for
334 elements showing high affinity for magnetite, and minimal for cations with the lowest abiotic
335 D^X (Fig. 6). This illustrates a screening effect induced by the bacterial membranes that limits

the transfer of cations distinct from Fe from the external solution to the location of magnetite formation regardless of the cation size and valence. Two exceptions are observed. Silver was more enriched in AMB-1 magnetite than the rest of the monovalent elements (Fig. 6A). This could reflect the antimicrobial properties of Ag(I)[31] and its sequestration into magnetite for detoxification as previously proposed for toxic cations[32]. Alternatively, such preferential inclusion of Ag in AMB-1 could arise from passive diffusion between the external solution and the intracellular medium. Additionally, Sr was more excluded from AMB-1 magnetite than other divalent elements (Fig. 6). Exposure to Sr was shown to induce efflux systems in bacteria[33], and Sr is known to disturb Ca metabolism in animals[34]. Low D^{Sr} might thus be generated by Sr pumping outside of the cell to maintain homeostasis.

Conclusion

The present contribution establishes an experimental and theoretical framework that can predict the behavior of trace and minor cations during synthetic magnetite formation based on their size, valence and unfilled 3d orbitals. This enabled us to elucidate the screening effect MTB have on biological magnetite formation. Beyond the geobiological interests for the identification of ancient terrestrial and extra-terrestrial life, our work has significant implications for nanotechnological applications of biological and/or abiotic nanoparticles of magnetite. Deliberate doping of trace and minor elements has been carried out to optimize magnetite nanoparticle composition for dedicated applications, including doping of Co and Zn that increase the efficiency of magnetite's magnetic properties for cancer treatment using hyperthermia[8,9,35], as well as its capacity of organic pollutant remediation and (bio)remediation of contaminated water[36–38]. The appropriateness of doped magnetite nanomaterials with tailored properties (e.g., magnetism) for future applications can be evaluated with our methodology by identifying the different outcomes of dopant composition via abiotic or biological synthesis.

Materials and Methods

Magnetite abiotic synthesis

Production of abiotic magnetite nanoparticles was performed using a titration device as already described[39]. An Fe chloride mixture ([Fe(II)Cl_2] = 0.33 M and [Fe(III)Cl_3] = 0.66 M) was added to a NaOH solution (pH = 11) at room-temperature. The decrease of pH associated with the release of protons during magnetite precipitation was compensated by adding additional NaOH solution (1 M) to keep the pH constant throughout the experiment. The doping elements were added at similar concentrations (100 ppb for each element) in the Fe mixture. The Fe mixture, NaOH solution, and the magnetite precipitation solution were kept under constant anoxic conditions by flushing N_2 to prevent Fe(II) oxidation. Magnetite samples were then recovered by centrifugation (8 000 rpm for 15 min), rinsed two times with Milli-Q water and dried in a desiccator. All samples were kept under anoxic conditions before XAS analyses.

Bacterial cultures and magnetite purification

The MSR-1 strain was cultivated under standard conditions following a previously published protocol[19]. Because MTB magnetite is strongly depleted in dopant elements compared to its abiotic counterpart[10], Mn, Co and Zn were added at higher concentration to maximize their incorporation into MSR-1 magnetite for XAS measurements. Doping elements were added at similar concentrations (33 μM for each element in the mixed-element condition, and 100 μM for single-doped samples) in MSR-1 growth medium. MSR-1 magnetite was then extracted for XAS and HR-ICP-MS analyses: MSR-1 bacteria were lysed using a French Press (3 runs at 7 000 kPa), recovered with a magnet, and purified with an EDTA-Triton-SDS preparation following a previously described procedure[10].

386 **Transmission electron microscopy**

387 Abiotic magnetite nanoparticles and MSR-1 bacteria were deposited on carbon-coated
388 copper grids for electron microscopy characterizations. MSR-1 grids were rinsed using Milli-
389 Q water to remove salts precipitated from the growth medium. Samples were then observed
390 with a FEI Tecnai G2 Biotwin microscope operating at 100 kV.

391

392 **Selection of trace and minor elements**

393 Four elements (B, Ca, K, Mg) from the initial work[10] were excluded for the present work: B
394 and K are contained in the glassware (borosilicates) used for the preparation and storage of
395 samples, and thus contaminate the magnetite and solution samples, while only one replicate
396 could be obtained in the case of Ca and Mg.

397

398 **Determination of element oxidation state in solution and magnetite**

399 The oxidation state of all doping trace and minor elements in precipitation solutions was
400 determined at the pH / E_h conditions representative of the abiotic precipitation solution and the
401 proposed magnetosome internal solution[40] with the geochemical code CHESS[41] using the
402 THERMODDEM[42] database. Because Fe(II) is found in octahedral sites in magnetite, all
403 divalent cations were considered as occupying octahedral sites in magnetite. Similarly, half of
404 Fe(III) is present in octahedral sites magnetite, the other half being contained in tetrahedral sites.
405 We thus considered trivalent cations to be incorporated in both 6- (50%) and 4-coordination
406 (50%).

407

408 **Prediction of trace and minor element partition coefficients from lattice strain theory**

409 The distribution of D^X values for an isovalent series of elements can be described by[16]:

410

$$D^X = D_{n+}^{0(M)} \times exp\left\{\frac{-4\pi N_A E_{n+}^M \left[\frac{1}{2} r_{n+}^{0(M)} \left(r^X - r_{n+}^{0(M)}\right)^2 + \frac{1}{3}\left(r^X - r_{n+}^{0(M)}\right)^3\right]}{RT}\right\} \quad (2)$$

With $D_{n+}^{0(M)}$ the partition coefficient for a fictive element with $r^X = r_{n+}^{0(M)}$ and causing no elastic strain (i.e. strain-compensated D^X), E_{n+}^M the lattice strain parameter describing the Young's Modulus (in GPa) of the site M, N_A the Avogadro's number, R the perfect gas constant, and T the temperature in Kelvin. Similarly, heterovalent cation substitution entail excess electric charge accommodated by the crystal lattice that will also translate into a penalty in energy for element incorporation[16]:

$$D_{n+}^{0(M)} = D^{00(M)} \times exp\left\{\frac{-N_A e^2 \left(Z^X - Z^{0(M)}\right)^2}{(2\varepsilon\rho RT)}\right\} \quad (3)$$

Where $D^{00(M)}$ is the strain-compensated partition coefficient for a fictive ion causing no electrostatic charging (i.e. homovalent substitution), e the electron charge, ρ the radius of the region over which the excess charge is distributed, ε the dielectric constant of that region, and Z^X and $Z^{0(M)}$ the ionic charge and the optimum ionic charge at the site M, respectively.

The parameters used for the calculation of predicted partition coefficients using Eq. 2 ($D_{n+}^{0(M)}$, $r_{n+}^{0(M)}$, and E_{n+}^M) are given in Table S3. Selected Young's modulus range between 85 and 470 GPa , which is in good agreement with the range of published values for macrocrystals and nanoparticles of magnetite[43–45]. Higher variability in E_{n+}^M than that observed here for magnetite has already been reported in many mineral phases, including plagioclase, diopside, augite, anorthite, albite, diopside or fluorite[46,47]. Such variability is related to the ion charge and the cation – oxygen distance[16]. In the case of magnetite, it can also be explained by the variability induced by the two lattice sites under consideration (tetrahedral and octahedral). For Eq. 3, a

dielectric constant (ε) of 50 and a lattice region with a radius (ρ) of 17 nm were considered (Fig. 3). Such values correspond to published ε for magnetite[48,49] and to the size of the magnetite nanoparticles produced for the determination of their trace element composition, respectively.

Inductively Coupled Plasma – Mass Spectrometry (ICP-MS) analyses

The concentrations of Fe, Mn, Co and Zn in the abiotic and MSR-1 magnetite nanoparticles, in the residual precipitation solution and in the residual bacterial growth media were determined using a Perkin Elmer NexIon 300X mass spectrometer (collision mode configuration with a Rh103 internal standard) at the *Centre Européen de Recherche et d'Enseignement en Géosciences de l'Environnement* (CEREGE Aix-en-Provence, France). Three replicates were performed for each experimental conditions.

X-ray Absorption Spectroscopy (XAS)

The abiotic and biological magnetite samples were measured under cryogenic conditions in powdered form. To prepare the samples for measurement, the purified abiotic and biological magnetite nanoparticles were spread onto Kapton tape and folded to seal the sample. The samples were kept frozen during storage, shipment and measurement. Principal data was collected at the I20-Scanning beamline (Diamond Light Source, Didcot, UK). Preliminary XAS data (additional Fe, Ni and Cu K-edge spectra) was collected at the Sector BM-20 beamline (Advanced Photon Source, Argonne National Laboratory, IL, USA). Due to the dilute nature of dopant metals, fluorescence detection was employed to collect XAS spectra. Several scans were collected and averaged to produce the spectra presented in this work. We note that Zn metal contamination (I20-Scanning data) was discovered after data collection and was attributed to a custom-printed sample holder used at the beamline. Linear combination fitting with a Zn metal reference accounts for this contribution. XAS data from Zn(II)-citrate and

Zn(II)-histadine complexes were implemented to fit as octahedral Zn(II) complexes. XAS of reference foils for Mn, Co and Zn were simultaneously collected downstream via ionization chambers for energy calibration. Athena and WinXAS programs were used for background subtraction, energy calibration, normalization and transformation to FT-EXAFS spectra. Athena was implemented for linear combination fitting and WinXAS for refined EXAFS fitting. The computational package FEFF8.2 was employed to simulate scattering paths for EXAFS fitting and to simulate Mn K-edge XANES of Mn in octahedral and tetrahedral lattice sites in magnetite.

Acknowledgements

MA is supported by a grant through the *Fondation pour la Recherche Médicale* (ARF201909009123). DMC acknowledges research funding through a European Union Marie-Skłodowska Curie Action International Fellowship (MSCA-IF Project 797431: BioNanoMagnets) and from a CNRS starting grant. CLS@APS facilities (Sector 20-BM) at the Advanced Photon Source (APS) are supported by the U.S. Department of Energy (DOE), NSERC Canada, the University of Washington, the Canadian Light Source (CLS), and the APS. Use of the APS is supported by the DOE under Contract No. DE-AC02−06CH11357. We acknowledge Diamond Light Source for beamtime on I20-Scanning under proposal SP25495. We thank the beamline scientists Michael Pape (APS) and Fred Mosselmans (DLS) for their technical assistance during beamtimes. The groups of Thomas N. Stokes, Alicia Muela and M. Luisa Fdez-Gubieda are thanked for sharing XAS data on ferrite references. Fred Mosselmans is also thanked for sharing Zn-based references. We thank Bernard Angeletti and Jean-Paul Ambrosi from the *Centre Européen de Recherche et d'Enseignement des Géosciences de l'Environnement (*Aix-en-Provence, France*)* for assistance with the mass spectrometry

483 measurements. We thank Paul N. Duchesne for constructive feedback and comments on the
484 manuscript.

References

(1) Usman, M.; Byrne, J. M.; Chaudhary, A.; Orsetti, S.; Hanna, K.; Ruby, C.; Kappler, A.; Haderlein, S. B. Magnetite and Green Rust: Synthesis, Properties, and Environmental Applications of Mixed-Valent Iron Minerals. *Chem. Rev.* **2018**, *118* (7), 3251–3304. https://doi.org/10.1021/acs.chemrev.7b00224.

(2) Uebe, R.; Schueler, D. Magnetosome Biogenesis in Magnetotactic Bacteria. *Nat. Rev. Microbiol.* **2016**, *14* (10), 621–637. https://doi.org/10.1038/nrmicro.2016.99.

(3) Lin, W.; Paterson, G. A.; Zhu, Q.; Wang, Y.; Kopylova, E.; Li, Y.; Knight, R.; Bazylinski, D. A.; Zhu, R.; Kirschvink, J. L.; Pan, Y. Origin of Microbial Biomineralization and Magnetotaxis during the Archean. *Proc. Natl. Acad. Sci. U. S. A.* **2017**, *114* (9), 2171–2176. https://doi.org/10.1073/pnas.1614654114.

(4) Amor, M.; Mathon, F. P.; Monteil, C. L.; Busigny, V.; Lefevre, C. T. Iron-Biomineralizing Organelle in Magnetotactic Bacteria: Function, Synthesis and Preservation in Ancient Rock Samples. *Environ. Microbiol.* **2020**, *22* (9), 3611–3632. https://doi.org/10.1111/1462-2920.15098.

(5) Plan Sangnier, A.; Preveral, S.; Curcio, A.; K A Silva, A.; Lefèvre, C. T.; Pignol, D.; Lalatonne, Y.; Wilhelm, C. Targeted Thermal Therapy with Genetically Engineered Magnetite Magnetosomes@RGD: Photothermia Is Far More Efficient than Magnetic Hyperthermia. *J Control Release* **2018**, *279*, 271–281. https://doi.org/10.1016/j.jconrel.2018.04.036.

(6) Felfoul, O.; Mohammadi, M.; Taherkhani, S.; de Lanauze, D.; Xu, Y. Z.; Loghin, D.; Essa, S.; Jancik, S.; Houle, D.; Lafleur, M.; Gaboury, L.; Tabrizian, M.; Kaou, N.; Atkin, M.; Vuong, T.; Batist, G.; Beauchemin, N.; Radzioch, D.; Martel, S. Magneto-Aerotactic Bacteria Deliver Drug-Containing Nanoliposomes to Tumour Hypoxic Regions. *Nat. Nanotechnol.* **2016**, *11* (11), 941–947. https://doi.org/10.1038/NNANO.2016.137.

(7) Zingsem, B. W.; Feggeler, T.; Terwey, A.; Ghaisari, S.; Spoddig, D.; Faivre, D.; Meckenstock, R.; Farle, M.; Winklhofer, M. Biologically Encoded Magnonics. *Nature Communications* **2019**, *10* (1), 4345. https://doi.org/10.1038/s41467-019-12219-0.

(8) Byrne, J. M.; Coker, V. S.; Moise, S.; Wincott, P. L.; Vaughan, D. J.; Tuna, F.; Arenholz, E.; van der Laan, G.; Pattrick, R. a. D.; Lloyd, J. R.; Telling, N. D. Controlled Cobalt Doping in Biogenic Magnetite Nanoparticles. *Journal of The Royal Society Interface* **2013**, *10* (83), 20130134. https://doi.org/10.1098/rsif.2013.0134.

(9) Byrne, J. M.; Coker, V. S.; Cespedes, E.; Wincott, P. L.; Vaughan, D. J.; Pattrick, R. A. D.; Laan, G. van der; Arenholz, E.; Tuna, F.; Bencsik, M.; Lloyd, J. R.; Telling, N. D. Biosynthesis of Zinc Substituted Magnetite Nanoparticles with Enhanced Magnetic Properties. *Advanced Functional Materials* **2014**, *24* (17), 2518–2529. https://doi.org/10.1002/adfm.201303230.

(10) Amor, M.; Busigny, V.; Durand-Dubief, M.; Tharaud, M.; Ona-Nguema, G.; Gélabert, A.; Alphandéry, E.; Menguy, N.; Benedetti, M. F.; Chebbi, I.; Guyot, F. Chemical Signature of Magnetotactic Bacteria. *Proc. Natl. Acad. Sci. U. S. A.* **2015**, *112* (6), 1699–1703. https://doi.org/10.1073/pnas.1414112112.

(11) Thomas-Keprta, K. L.; Bazylinski, D. A.; Kirschvink, J. L.; Clemett, S. J.; McKay, D. S.; Wentworth, S. J.; Vali, H.; Gibson, E. K.; Romanek, C. S. Elongated Prismatic Magnetite Crystals in ALH84001 Carbonate Globules: Potential Martian Magnetofossils. *Geochim. Cosmochim. Acta* **2000**, *64* (23), 4049–4081. https://doi.org/10.1016/S0016-7037(00)00481-6.

(12) Thomas-Keprta, K. L.; Clemett, S. J.; McKay, D. S.; Gibson, E. K.; Wentworth, S. J. Origins of Magnetite Nanocrystals in Martian Meteorite ALH84001. *Geochim. Cosmochim. Acta* **2009**, *73* (21), 6631–6677. https://doi.org/10.1016/j.gca.2009.05.064.

(13) Golden, D. C.; Ming, D. W.; Schwandt, C. S.; Lauer, H. V.; Socki, R. A.; Morris, R. V.; Lofgren, G. E.; McKay, G. A. A Simple Inorganic Process for Formation of Carbonates, Magnetite, and Sulfides in Martian Meteorite ALH84001. *Am. Miner.* **2001**, *86* (3), 370–375.
(14) Jimenez-Lopez, C.; Rodriguez-Navarro, C.; Rodriguez-Navarro, A.; Perez-Gonzalez, T.; Bazylinski, D. A.; Lauer, H. V.; Romanek, C. S. Signatures in Magnetites Formed by (Ca,Mg,Fe)CO3 Thermal Decomposition: Terrestrial and Extraterrestrial Implications. *Geochim. Cosmochim. Acta* **2012**, *87*, 69–80. https://doi.org/10.1016/j.gca.2012.03.028.
(15) Muñoz, D.; Marcano, L.; Martín-Rodríguez, R.; Simonelli, L.; Serrano, A.; García-Prieto, A.; Fdez-Gubieda, M. L.; Muela, A. Magnetosomes Could Be Protective Shields against Metal Stress in Magnetotactic Bacteria. *Sci Rep* **2020**, *10* (1), 11430. https://doi.org/10.1038/s41598-020-68183-z.
(16) Blundy, J.; Wood, B. Partitioning of Trace Elements between Crystals and Melts. *Earth Planet. Sci. Lett.* **2003**, *210* (3–4), 383–397. https://doi.org/10.1016/S0012-821X(03)00129-8.
(17) Burns, R. G. *Mineralogical Applications of Crystal Field Theory*; Cambridge University Press, 1993.
(18) McClure, D. S. The Distribution of Transition Metal Cations in Spinels. *Journal of Physics and Chemistry of Solids* **1957**, *3* (3), 311–317. https://doi.org/10.1016/0022-3697(57)90034-3.
(19) Heyen, U.; Schuler, D. Growth and Magnetosome Formation by Microaerophilic Magnetospirillum Strains in an Oxygen-Controlled Fermentor. *Appl. Microbiol. Biotechnol.* **2003**, *61* (5–6), 536–544. https://doi.org/10.1007/s00253-002-1219-x.
(20) Tsvetkov, M.; Milanova, M.; Ivanova, I.; Neov, D.; Cherkezova-Zheleva, Z.; Zaharieva, J.; Abrashev, M. Phase Composition and Crystal Structure Determination of Cobalt Ferrite, Modified with Ce, Nd and Dy Ions by X-Ray and Neutron Diffraction. *Journal of Molecular Structure* **2019**, *1179*, 233–241. https://doi.org/10.1016/j.molstruc.2018.07.083.
(21) Amiri, S.; Shokrollahi, H. The Role of Cobalt Ferrite Magnetic Nanoparticles in Medical Science. *Materials Science and Engineering: C* **2013**, *33* (1), 1–8. https://doi.org/10.1016/j.msec.2012.09.003.
(22) Stokes, T. N.; Bromiley, G. D.; Gatta, G. D.; Rotiroti, N.; Potts, N. J.; Saunders, K. Cation Distribution and Valence in Synthetic Al–Mn–O and Fe–Mn–O Spinels under Varying Conditions. *Mineralogical Magazine* **2018**, *82* (4), 975–992. https://doi.org/10.1180/mgm.2018.109.
(23) Swatsitang, E.; Phokha, S.; Hunpratub, S.; Usher, B.; Bootchanont, A.; Maensiri, S.; Chindaprasirt, P. Characterization and Magnetic Properties of Cobalt Ferrite Nanoparticles. *Journal of Alloys and Compounds* **2016**, *664*, 792–797. https://doi.org/10.1016/j.jallcom.2015.12.230.
(24) Nakagomi, F.; da Silva, S. W.; Garg, V. K.; Oliveira, A. C.; Morais, P. C.; Franco Júnior, A.; Lima, E. C. D. The Influence of Cobalt Population on the Structural Properties of CoxFe3−xO4. *Journal of Applied Physics* **2007**, *101* (9), 09M514. https://doi.org/10.1063/1.2712821.
(25) Staniland, S.; Williams, W.; Telling, N.; Van der Laan, G.; Harrison, A.; Ward, B. Controlled Cobalt Doping of Magnetosomes in Vivo. *Nat. Nanotechnol.* **2008**, *3* (3), 158–162. https://doi.org/10.1038/nnano.2008.35.
(26) Marcano, L.; Muñoz, D.; Martín-Rodríguez, R.; Orue, I.; Alonso, J.; García-Prieto, A.; Serrano, A.; Valencia, S.; Abrudan, R.; Fernández Barquín, L.; García-Arribas, A.; Muela, A.; Fdez-Gubieda, M. L. Magnetic Study of Co-Doped Magnetosome Chains. *J. Phys. Chem. C* **2018**, *122* (13), 7541–7550. https://doi.org/10.1021/acs.jpcc.8b01187.
(27) Chalmin, E.; Farges, F.; Brown, G. E. A Pre-Edge Analysis of Mn K-Edge XANES Spectra to Help Determine the Speciation of Manganese in Minerals and Glasses. *Contrib*

584 *Mineral Petrol* **2009**, *157* (1), 111–126. https://doi.org/10.1007/s00410-008-0323-z.
585 (28) Carta, D.; Casula, M. F.; Floris, P.; Falqui, A.; Mountjoy, G.; Boni, A.; Sangregorio,
586 C.; Corrias, A. Synthesis and Microstructure of Manganese Ferrite Colloidal Nanocrystals.
587 *Phys. Chem. Chem. Phys.* **2010**, *12* (19), 5074–5083. https://doi.org/10.1039/B922646J.
588 (29) Toksha, B. G.; Shirsath, S. E.; Mane, M. L.; Patange, S. M.; Jadhav, S. S.; Jadhav, K.
589 M. Autocombustion High-Temperature Synthesis, Structural, and Magnetic Properties of
590 CoCrxFe2–XO4 ($0 \leq x \leq 1.0$). *J. Phys. Chem. C* **2011**, *115* (43), 20905–20912.
591 https://doi.org/10.1021/jp205572m.
592 (30) Giri, A. K.; Kirkpatrick, E. M.; Moongkhamklang, P.; Majetich, S. A.; Harris, V. G.
593 Photomagnetism and Structure in Cobalt Ferrite Nanoparticles. *Appl. Phys. Lett.* **2002**, *80*
594 (13), 2341–2343. https://doi.org/10.1063/1.1464661.
595 (31) Hsueh, Y.-H.; Lin, K.-S.; Ke, W.-J.; Hsieh, C.-T.; Chiang, C.-L.; Tzou, D.-Y.; Liu, S.-
596 T. The Antimicrobial Properties of Silver Nanoparticles in Bacillus Subtilis Are Mediated by
597 Released Ag+ Ions. *PLOS ONE* **2015**, *10* (12), e0144306.
598 https://doi.org/10.1371/journal.pone.0144306.
599 (32) Komeili, A. Molecular Mechanisms of Compartmentalization and Biomineralization
600 in Magnetotactic Bacteria. *Fems Microbiol. Rev.* **2012**, *36* (1), 232–255.
601 https://doi.org/10.1111/j.1574-6976.2011.00315.x.
602 (33) Brown, S. D.; Martin, M.; Deshpande, S.; Seal, S.; Huang, K.; Alm, E.; Yang, Y.; Wu,
603 L.; Yan, T.; Liu, X.; Arkin, A.; Chourey, K.; Zhou, J.; Thompson, D. K. Cellular Response of
604 Shewanella Oneidensis to Strontium Stress. *Applied and Environmental Microbiology* **2006**,
605 *72* (1), 890–900. https://doi.org/10.1128/AEM.72.1.890-900.2006.
606 (34) Corradino, R. A.; Ebel, J. G.; Craig, P. H.; Taylor, A. N.; Wasserman, R. H. Calcium
607 Absorption and the Vitamin D3-Dependent Calcium-Binding Protein. *Calc. Tis Res.* **1971**, *7*
608 (1), 81–92. https://doi.org/10.1007/BF02062596.
609 (35) Alphandery, E.; Carvallo, C.; Menguy, N.; Chebbi, I. Chains of Cobalt Doped
610 Magnetosomes Extracted from AMB-1 Magnetotactic Bacteria for Application in Alternative
611 Magnetic Field Cancer Therapy. *J. Phys. Chem. C* **2011**, *115* (24), 11920–11924.
612 https://doi.org/10.1021/jp201274g.
613 (36) Fazli, A.; Khataee, A.; Brigante, M.; Mailhot, G. Cubic Cobalt and Zinc Co-Doped
614 Magnetite Nanoparticles for Persulfate and Hydrogen Peroxide Activation towards the
615 Effective Photodegradation of Sulfalene. *Chem. Eng. J.* **2021**, *404*, 126391.
616 https://doi.org/10.1016/j.cej.2020.126391.
617 (37) Huber, F.; Schild, D.; Vitova, T.; Rothe, J.; Kirsch, R.; Schaefer, T. U(VI) Removal
618 Kinetics in Presence of Synthetic Magnetite Nanoparticles. *Geochim. Cosmochim. Acta* **2012**,
619 *96*, 154–173. https://doi.org/10.1016/j.gca.2012.07.019.
620 (38) Crean, D. E.; Coker, V. S.; van der Laan, G.; Lloyd, J. R. Engineering Biogenic
621 Magnetite for Sustained Cr(VI) Remediation in Flow-through Systems. *Environ. Sci. Technol.*
622 **2012**, *46* (6), 3352–3359. https://doi.org/10.1021/es2037146.
623 (39) Baumgartner, J.; Carillo, M. A.; Eckes, K. M.; Werner, P.; Faivre, D. Biomimetic
624 Magnetite Formation: From Biocombinatorial Approaches to Mineralization Effects.
625 *Langmuir* **2014**, *30* (8), 2129–2136. https://doi.org/10.1021/la404290c.
626 (40) Eguchi, Y.; Fukumori, Y.; Taoka, A. Measuring Magnetosomal PH of the
627 Magnetotactic Bacterium Magnetospirillum Magneticum AMB-1 Using PH-Sensitive
628 Fluorescent Proteins. *Biosci. Biotechnol. Biochem.* **2018**, *82* (7), 1243–1251.
629 https://doi.org/10.1080/09168451.2018.1451739.
630 (41) Van der Lee, J.; De Windt, L. CHESS Tutorial and Cookbook. Updated for Version
631 3.0, Manual Nr. LHM/RD/02/13.; Paris, 2002; p 116.
632 (42) Blanc, P.; Lassin, A.; Piantone, P.; Azaroual, M.; Jacquemet, M.; Fabbri, A.; Gaucher,
633 E. C. Thermoddem: A Geochemical Database Focused on Low Temperature Water/Rock

Interactions and Waste Materials. *Appl. Geochem.* **2012**, *27* (10), 2107–2116. https://doi.org/10.1016/j.apgeochem.2012.06.002.
(43) Chicot, D.; Mendoza, J.; Zaoui, A.; Louis, G.; Lepingle, V.; Roudet, F.; Lesage, J. Mechanical Properties of Magnetite (Fe3O4), Hematite (Alpha-Fe2O3) and Goethite (Alpha-FeO Center Dot OH) by Instrumented Indentation and Molecular Dynamics Analysis. *Mater. Chem. Phys.* **2011**, *129* (3), 862–870. https://doi.org/10.1016/j.matchemphys.2011.05.056.
(44) Fine, M. E.; Kenney, N. T. Moduli and Internal Friction of Magnetite as Affected by the Low-Temperature Transformation. *Phys. Rev.* **1954**, *94* (6), 1573–1576. https://doi.org/10.1103/PhysRev.94.1573.
(45) Gholizadeh, A. A Comparative Study of Physical Properties in Fe3O4 Nanoparticles Prepared by Coprecipitation and Citrate Methods. *J. Am. Ceram. Soc.* **2017**, *100* (8), 3577–3588. https://doi.org/10.1111/jace.14896.
(46) Blundy, J.; Wood, B. Prediction of Crystal-Melt Partition-Coefficients from Elastic-Moduli. *Nature* **1994**, *372* (6505), 452–454. https://doi.org/10.1038/372452a0.
(47) van Hinsberg, V. J.; Migdisov, A. A.; Williams-Jones, A. E. Reading the Mineral Record of Fluid Composition from Element Partitioning. *Geology* **2010**, *38* (9), 847–850. https://doi.org/10.1130/G31112.1.
(48) Pimenov, A.; Tachos, S.; Rudolf, T.; Loidl, A.; Schrupp, D.; Sing, M.; Claessen, R.; Brabers, V. A. M. Terahertz Conductivity at the Verwey Transition in Magnetite. *Phys. Rev. B* **2005**, *72* (3), 035131. https://doi.org/10.1103/PhysRevB.72.035131.
(49) Zulfiqar; Afzal, S.; Khan, R.; Zeb, T.; Rahman, M. ur; Burhanullah; Ali, S.; Khan, G.; Rahman, Z. ur; Hussain, A. Structural, Optical, Dielectric and Magnetic Properties of PVP Coated Magnetite (Fe3O4) Nanoparticles. *J Mater Sci: Mater Electron* **2018**, *29* (23), 20040–20050. https://doi.org/10.1007/s10854-018-0134-6.
(50) Shannon, R. D.; Prewitt, C. T. Effective Ionic Radii in Oxides and Fluorides. *Acta Crystallographica Section B* **1969**, *25* (5), 925–946. https://doi.org/10.1107/S0567740869003220.

Figures

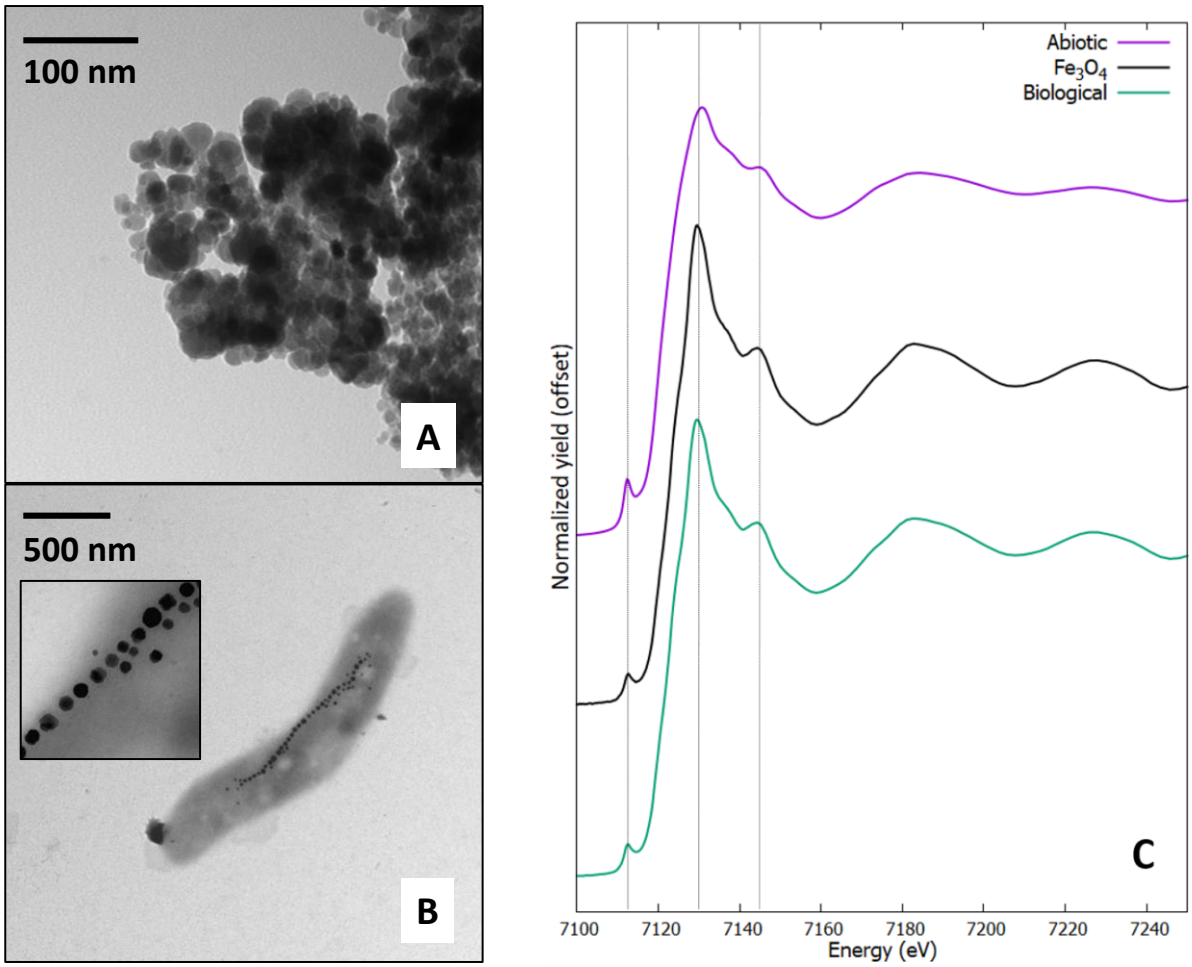

Figure 1. Transmission electron microscopy images of (A) abiotic magnetite nanoparticles and (B) MSR-1 bacteria containing magnetite nanoparticles in magnetosomes (inset, magnified region of magnetosome chain). (C) Fe K-edge X-ray absorption near-edge structure spectra of abiotic and biological magnetite nanoparticles with magnetite reference.

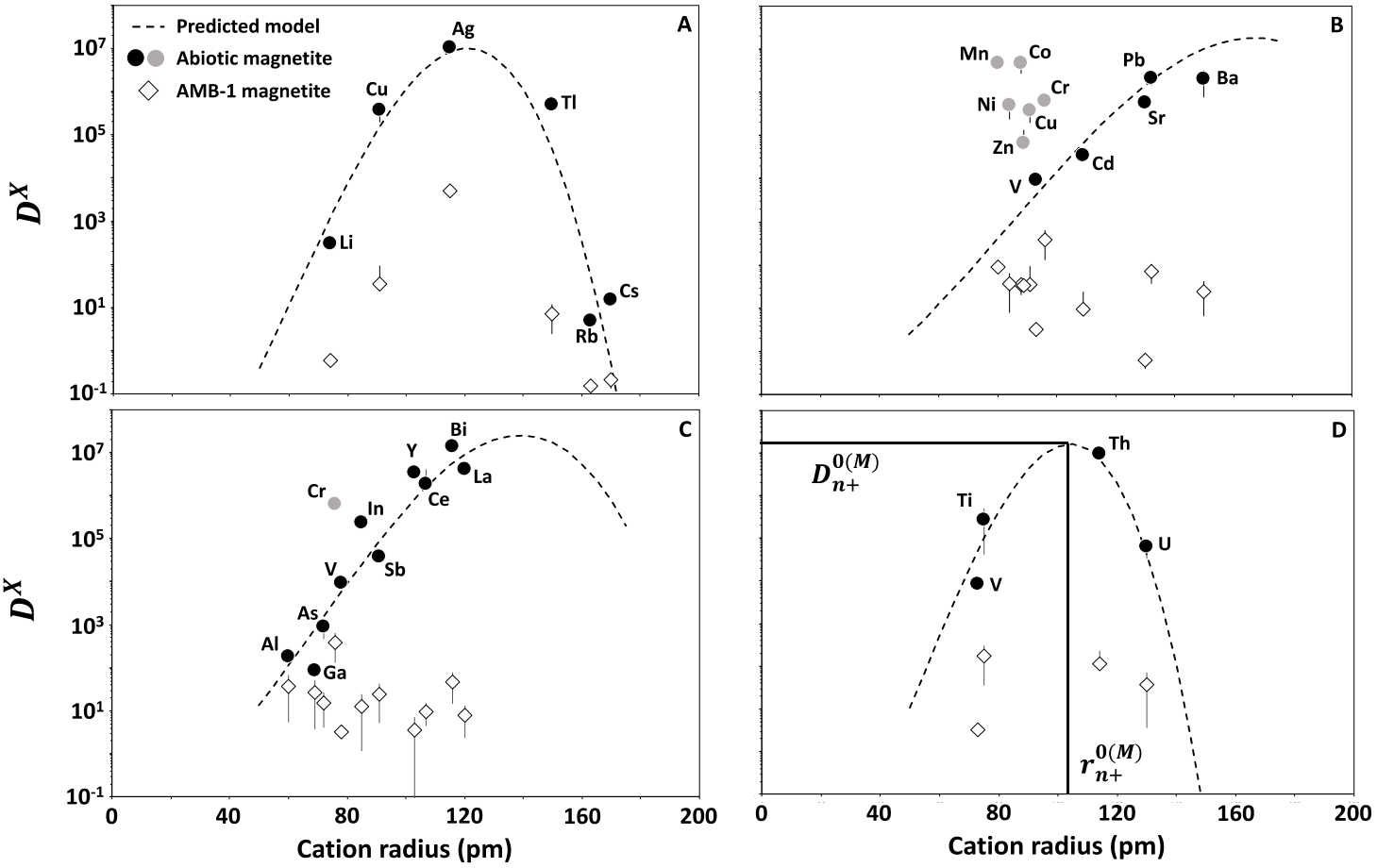

Figure 2. Partition coefficients (D^X) of (A) monovalent, (B) divalent, (C) trivalent and (D) tetravalent cations in the case of abiotic (black and grey circles) and biological (AMB-1, open diamonds) magnetite. Dashed line indicate the predicted values of D^X based on a lattice strain model (Eq. 2). Grey symbols point to 3d metals [Co(II), Cr(II), Cr(III), Cu(II), Mn(II), Ni(II), Zn(II)] showing variations from the predicted values in the abiotic precipitation of magnetite. Cation radius taken from Shannon and Prewitt and summarized in Table S7[50]. Black lines in (D) indicate the position of ideal cation radius ($r_{n+}^{0(M)}$) and strain-compensated partition coefficient ($D_{n+}^{0(M)}$).

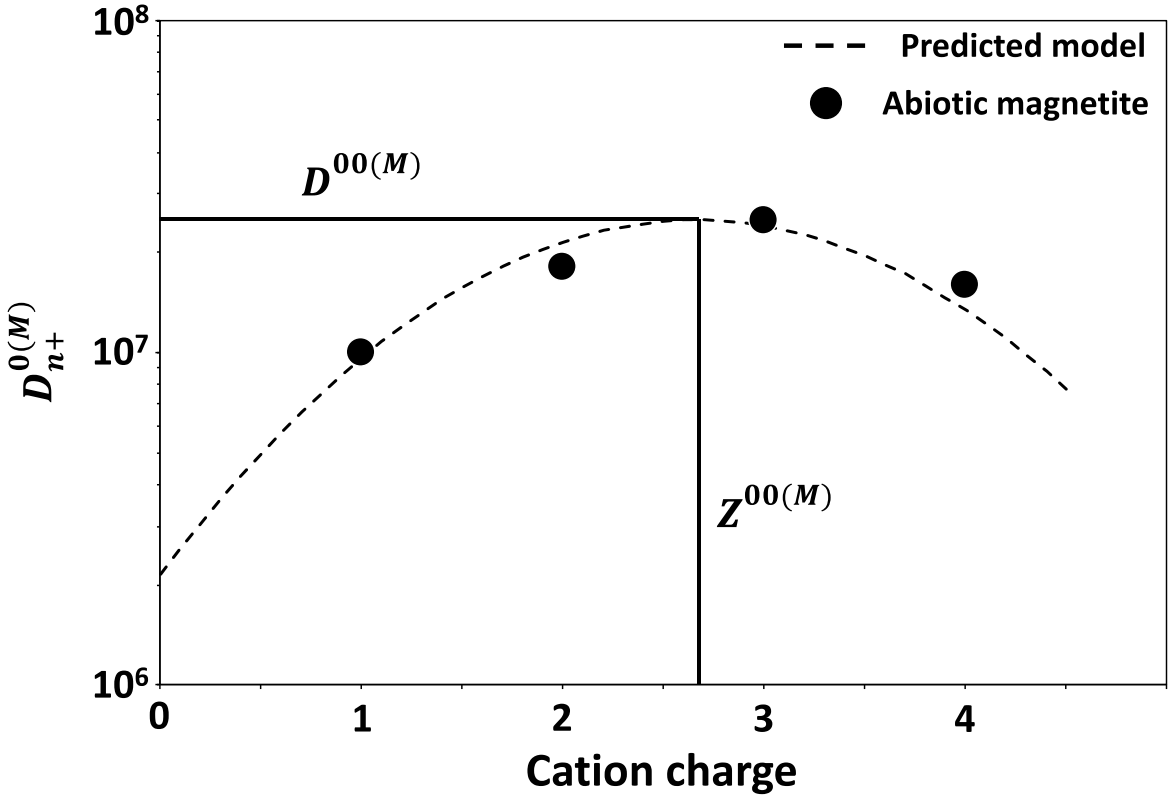

Figure 3. Strain-compensated partition coefficients ($D_{n+}^{0(M)}$) for each element valence extracted from Figs. 2A to 2D. The predicted model was calculated using Eq. 3 and considering published values of magnetite's dielectric constant of 50 and a lattice region with a radius of 17 nm corresponding to the size of magnetite nanoparticles (see Materials and Methods for details). Black lines indicate the position of ideal charge ($Z^{00(M)}$) and strain-compensated partition coefficient causing no electrostatic charging ($D^{00(M)}$).

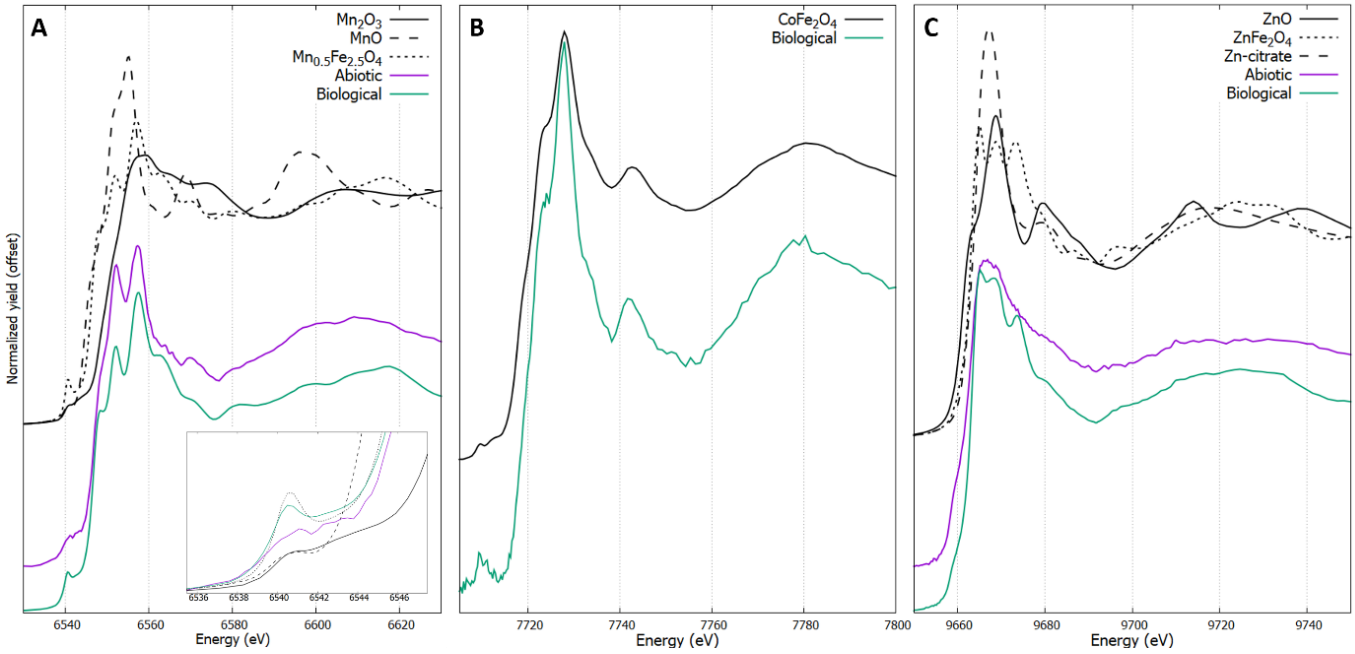

Figure 4. X-ray absorption near edge structure (XANES) of doped abiotic and biological magnetite nanoparticles with reference materials at (A) Mn K-edge (inset, pre-edge region), (B) Co K-edge and (C) Zn K-edge.

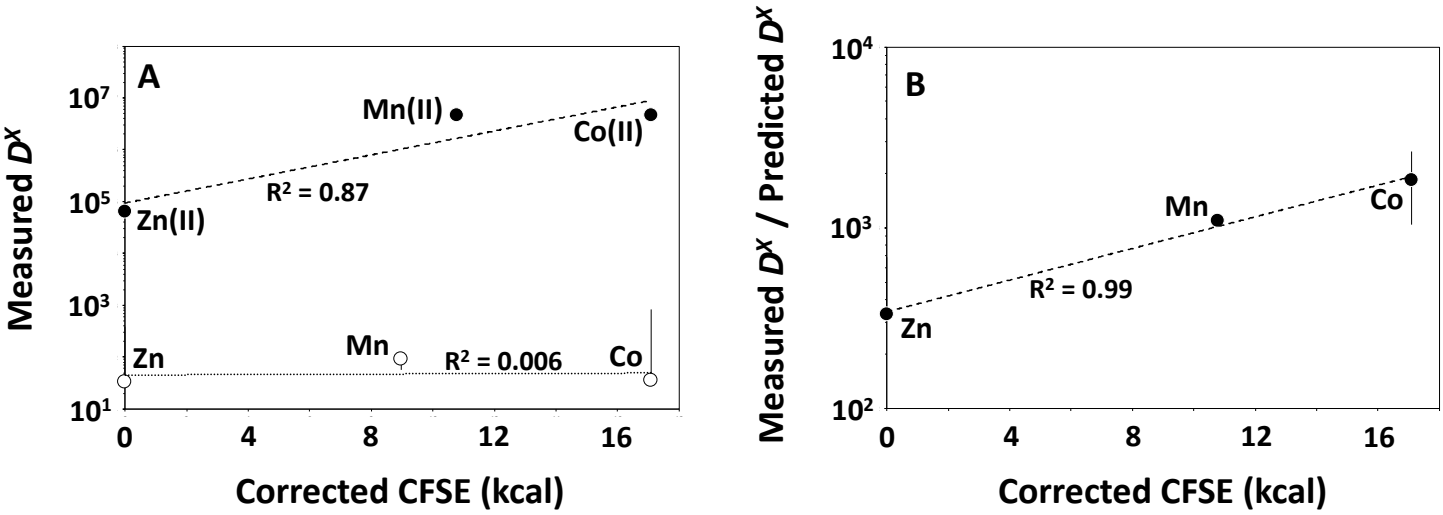

Figure 5. (A) Partition coefficients (D^X) and (B) ratio of measured partition coefficients and partition coefficients predicted from a lattice strain theory (Eq. 2) of Mn, Co and Zn represented against their XAS-corrected Crystal Field Stabilization Energy (CFSE). Black and open symbols represent abiotic and biological conditions, respectively.

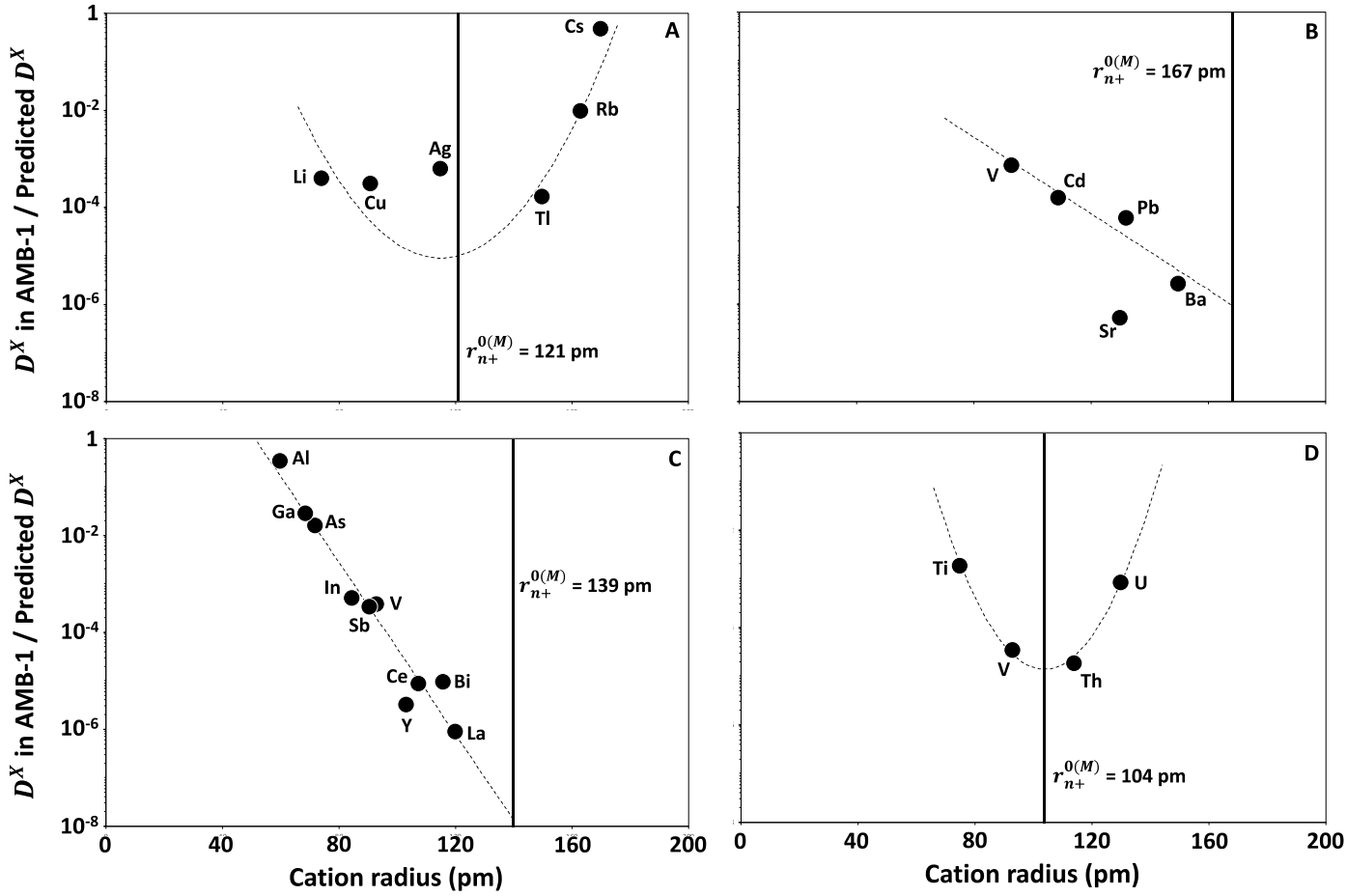

Figure 6. Biological D^X obtained from AMB-1 cultures normalized to the D^X predicted from lattice strain theory (Eq. 2) in the case of (A) monovalent, (B) divalent, (C) trivalent and (D) tetravalent elements. $r_{n+}^{0(M)}$ values reported here are extracted from Fig. 2 and Table S3.